ACS APPLIED NANO MATERIALS

www.acsanm.org

Article

Fabrication of Mono- and Multilayered Large-Area Ultrathin Polymer Nanocomposite Films: Implications for Functional Nanoparticle Applications

G. Cristian Vásquez,* Martin Dulle, Beate Förster, Margarita Kruteva, Sascha Ehlert, and Stephan Förster*

Cite This: *ACS Appl. Nano Mater.* 2023, 6, 22651−22659

Read Online

ACCESS | Metrics & More | Article Recommendations | Supporting Information

ABSTRACT: Ultrathin polymer nanocomposite films are gaining importance in electronic, optical, magnetic, or sensor devices with widespread applications in the areas of electronics, information technology, and medicine. Future developments in ultrathin nanocomposite films require the fabrication of ever thinner films with controllable thickness, homogeneous nanoparticle distribution, and large areas. We here demonstrate a dip-coating-delamination method to prepare ultrathin and large-area polymer nanocomposite films on various substrates or as free-standing films. We demonstrate thickness control in the range between 17 and 150 nm, controlled via film withdrawing speed and nanoparticle volume fraction. Ultrathin films with magnetic, semiconductor, and down-conversion nanoparticles having spherical, rod-like, or platelet shapes can be prepared. We show that the magnetic and optical properties of the nanoparticles are well preserved by the fabrication method. Furthermore, we demonstrate the assembly of ultrathin large-area hetero multilayer nanocomposite films. This method thus provides a versatile, well-controllable, and scalable method to prepare supported or free-standing multifunctional large-area ultrathin nanocomposite films with low material consumption.

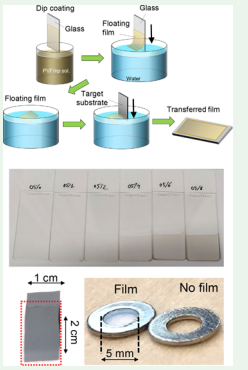

KEYWORDS: *nanoparticles, nanocomposites, PVF, self-assembly, ultrathin films, multilayers*

INTRODUCTION

Nanocomposites combine the ease of fabrication, the mechanical properties, and the scalability of polymers with the excellent electronic, optical, and magnetic properties of nanoparticles. For many applications, nanocomposites are applied as thin films, e.g., in electronic, optical, magnetic, or sensor devices, with widespread applications in the areas of optoelectronics, information technology, and medicine.[1−5] A continuous challenge is to fabricate ever thinner films, down to single nanoparticle layer films, e.g., for bendable and flexible devices in related emerging application fields.[4,6,7] Therefore, methods are needed toward the fabrication of ultrathin nanocomposite films, with controllable thickness, homogeneous nanoparticle distribution, and large areas (i.e., high aspect ratio), as supported or even free-standing films.

Thin polymer films with thicknesses below 100 nm are usually prepared via layer-by-layer assembly,[8,9] spin-coating,[10,11] transfer-printing,[4,12] or flow-coating techniques.[13] Flow-coating has been developed by Stafford et al.[13] and allows the preparation of nanoscale thin films with constant or a gradient film thickness[14] and has been applied to the preparation of nanoparticle coatings.[15,16] Recent research has also focused on innovative strategies for thin and free-standing films, such as in situ synthesis in liquid/liquid interfacial polymerization.[17,18] These methods generally offer precise control over the film composition and thickness but are not very efficient for multilayer assembly, requiring the combination of different deposition methods, raising the number of parameters to control. Spin-coating is a well-established thin-film fabrication technique. It has recently been combined with a delamination technique to prepare polymer films with thicknesses down to 8 nm.[10] These ultrathin films were prepared by spin-coating onto polydiallyldimethylammonium chloride (PDAC)-functionalized silicon wafers and subsequently delaminated in water.[19,20] The method has been established for polystyrene and poly(methyl methacrylate), as well as for polyvinyl formal (PVF).[10] PVF is a polymer with excellent stability[21,22] and mechanical properties,[10,23] which has been used as electrical insulation coatings and as ion-conducting membranes for Li batteries.[23,24] With the spin-coating/delamination technique, large-area ultrathin PVF films could be fabricated for thin-film capacitors,[25] organic light-emitting diodes,[20] and organic field effect transistors.[26]

It has been demonstrated that PVF can be used to prepare nanocomposites such as for PVF/TiO_2 and PVF/ZnO nano-

Received: June 24, 2023
Revised: October 31, 2023
Accepted: November 9, 2023
Published: December 8, 2023

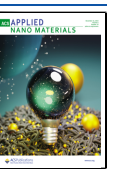

composites for sensors and detectors.[21,27] Interestingly, PVF is routinely used as thin support films for TEM specimen grids, where the films are prepared by a simple dip-coating/delamination technique using glass substrates. Therefore, it would be highly interesting to investigate whether this method can be adapted to fabricate ultrathin, large-area PVF nanocomposite films. Compared to spin-coating, both flow-coating and dip-coating have a striking advantage of a low material consumption; meanwhile, both methods allow the straightforward fabrication of multilayers. Thus, it is more economical with respect to material consumption and versatility. If ultrathin-film PVF nanocomposite films could be prepared via this simple dip-coating/delamination technique, this would provide a way to the efficient and controlled fabrication of ultrathin nanocomposite films for widespread applications.

Here, we show that it is indeed possible to fabricate ultrathin nanocomposite films by this simple dip-coating/delamination method, even with unfunctionalized standard glass slides. We fabricated various PVF-based nanocomposite films with controllable thicknesses between 17 and 150 nm, homogeneous nanoparticle distribution, and large areas. The large-area and free-standing films are feasibly transferred onto various substrates, where the presence of small particles favors the formation and delamination of thinner films. We demonstrate the applicability of the method by the fabrication of ultrathin nanocomposite films with magnetic, luminescent, semiconducting, and down-conversion nanoparticles having spherical, rod-like, or platelet shapes. In addition, we demonstrate the assembly of large-area hetero multilayer nanocomposite films. This method thus provides a controllable, versatile, and scalable method to prepare multifunctional large-area and ultrathin nanocomposite films with low materials consumption.

RESULTS AND DISCUSSION

Supported and Free-Standing Nanocomposite Ultrathin Film Preparation. For full details on the nanocomposite films, see the Experimental Section in the Supporting Information. To prepare the nanocomposite solutions, a PVF stock solution was mixed with certain amounts of nanoparticles dispersed in chloroform and diluted until the PVF concentration was reduced down to 0.5 wt % (7.5 mg/mL).

For the initial series of nanocomposites, oleic acid-coated iron oxide nanoparticles (OA-FeO_x) were used as nanoparticles. If not specified, the dip-coating parameters, i.e., immersion speed, dwell time, and withdrawal speed, were 20, 10, and 0.5 mm/s, respectively. At these conditions, a 2.5 × 2.5 cm^2 film can be deposited in 1 min. After a drying time of 10−15 min, the films can be delaminated onto the air/water interface (see Figure S1a,b). The free-floating films can subsequently be collected with the target substrate (e.g., Si), as represented in the scheme in Figure 1a. The nanoparticle density in the thin films prepared by dip-coating is proportional to the nanoparticle concentration in solution and depends on the deposition conditions. The films are therefore labeled as the np concentration in the solutions in mg/mL.

We note that the oleic acid shell results from the nanoparticle synthesis, where oleic acid stabilizes the nanoparticles against aggregation during the nucleation and growth phases and in their final state. The oleic acid shell remains on the nanoparticles to keep them well dispersed in organic solvents. The oleic acid shell does not play a role during the delamination and transferring process other than stabilizing the nanoparticles.

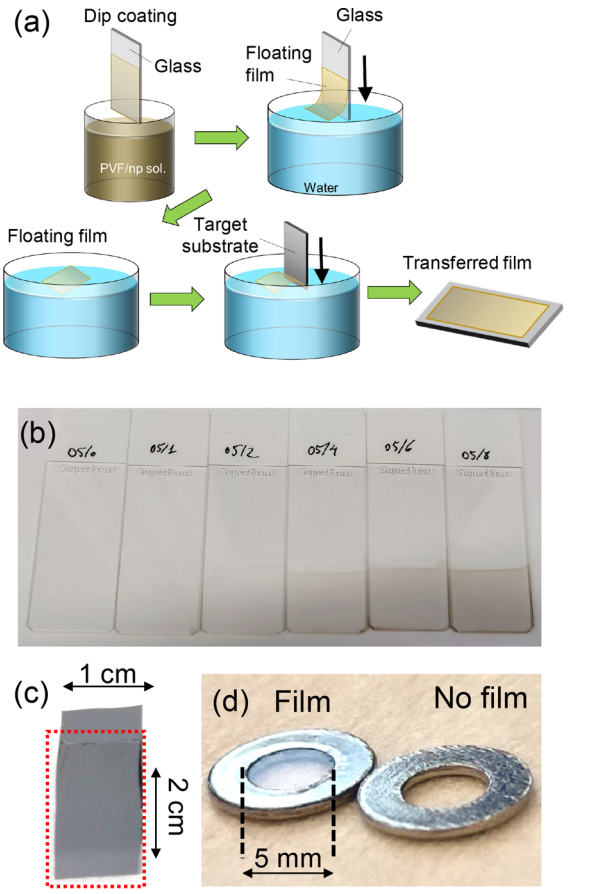

Figure 1. (a) Scheme of the thin-film preparation and transfer method. (b) As-deposited films on glass substrates. (c) Nanocomposite film (1 mg/mL) transferred onto a Si substrate. (d) A single free-standing nanocomposite layer (8 mg/mL) supported on an aluminum O-ring. The thickness of the films in (c) and (d) is ∼40−50 nm.

Figure 1b shows a series of as-deposited nanocomposite films on glass slides (parent substrates) with increasing nanoparticle concentrations from 0.5 to 8 mg/mL. The increased particle density in the films is noticeable by the progressive darkening with increasing nanoparticle concentration. It is important to highlight the great homogeneity achieved even for np concentrations of 6 or 8 mg/mL (see also Figure S1c), which correspond to approximately 1:1 weight ratio of PVF/nanoparticle in the nanocomposite solution. In addition, the method allows to transfer the ultrathin nanocomposite films onto flat rigid substrates such as a Si wafer, as shown in Figure 1c, onto a thinner and bendable TEM grid (shown later), or even to a more unconventional substrate such as simply an aluminum O-ring to prepare a large-area free-standing film, as shown in Figure 1d.

Thickness Control. The thickness of the nanocomposite films can be controlled by the withdrawal speed of the glass substrate during the final dip-coating step. The thickness of the films transferred onto the Si substrates was measured by X-ray reflectometry (XRR). The XRR intensity curves depicted in Figure 2a were measured for pure PVF films dip-coated at withdrawal speeds from 0.03 up to 10 mm/s. The measured XRR intensities show well-defined interference oscillations (Kiessig fringes)[28] from which the thickness can be determined. For a full quantitative analysis, the XRR intensities were simulated assuming refined substrate/film density profiles.[29] For the PVF layers on Si substrates, we assumed a thin native SiO_2

https://doi.org/10.1021/acsanm.3c02820
ACS Appl. Nano Mater. 2023, 6, 22651−22659

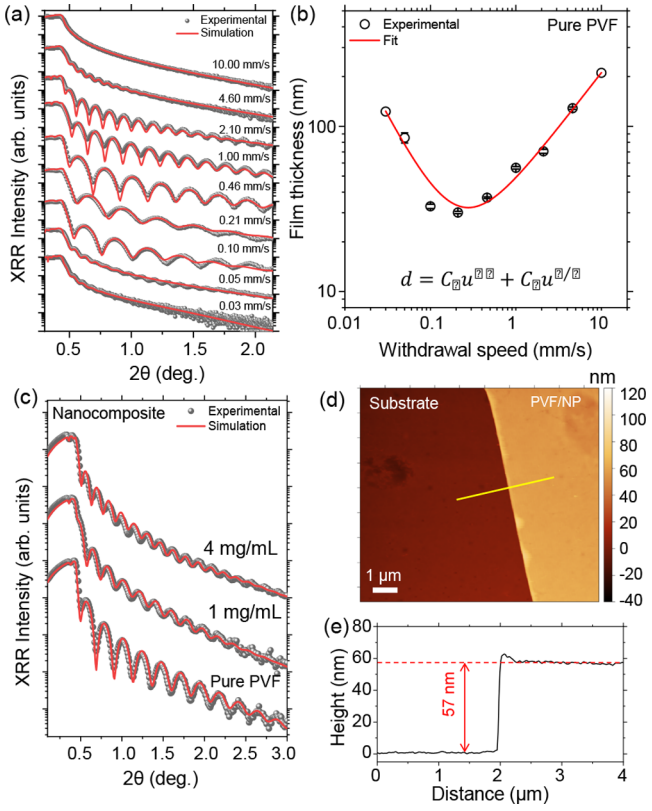

Figure 2. (a) Experimental and simulated X-ray reflectometry (XRR) profiles for pure PVF films deposited and transferred at different withdrawal speeds. (b) The calculated thicknesses and curve fit to eq 1. (c) Experimental and simulated XRR profiles for pure PVF and nanocomposites with different concentrations of OA-coated FeO_x nanoparticles deposited at 0.5 mm/s withdrawal speed. (d) AFM topography scan from the film edge of a film from 0.5 wt % PVF and 1.0 mg/mL nanoparticle concentration. (e) Line-scan profile across the edge marked by the line in (d).

interlayer of 1.5 nm thickness. The XRR analysis shows that the PVF films are smooth and uniform on large length scales, showing interference colors (see Figure S2a), with a remarkably small mean roughness (σ) of the order of 1 nm for films deposited at 0.1−2.0 mm/s.

Figure 2b shows the thickness d as measured by XRR as a function of withdrawal speed u. It shows a systematic variation of the thickness in a range from 30 to 200 nm and a good reproducibility of the film preparation method. The dependence of the thickness on the withdrawal speed can be described by the equation[30]

$$d = k_i\left(\frac{E}{L}u^{-1} + Du^{2/3}\right) \quad (1)$$

where E is the solvent evaporation rate, L is the substrate width, D is a global constant related to the fluid properties of the solution, and k_i is a materials constant defined by $k_i = c_iM_i/\alpha_i\rho_i$, where c is the material concentration, M is the molar weight, α is the volume fraction or porosity, and ρ is the materials density. The solid line in Figure 2b shows a corresponding fit to the equation $d = C_1u^{-1} + C_2u^{2/3}$ showing good agreement with eq 1. The V shape of the curve is due to a competition of the capillary (dominating at slow speed) and draining regimes (dominating at higher speed) that define the film thickness of the dip-coated films.[31,32] The optimal value of the withdrawal speed to obtain the minimum thickness is found to be ca. 0.25 mm/s. For the preparation of ultrathin nanocomposite films, we selected a withdrawal speed of 0.5 mm/s to ensure that atmospheric conditions are constant during coating, and hence guarantee minimal effect on the film quality.[31] Overall, the nanocomposites present a similar trend of the thickness as a function of the withdrawal speed, as shown in Figure S2b−d.

For the thin nanocomposite films, there is an additional influence of the nanoparticle concentration. The XRR intensities depicted in Figure 2c were measured for pure PVF and for PVF/OA-FeO_x nanocomposite films with 1 and 4 mg/mL nanoparticle concentrations. The main parameters obtained from the simulated profiles are summarized in Table 1. For the pure PVF film, the thickness determined by XRR was 37 nm, while for the PVF/OA-FeO_x nanocomposite films, it was 46 and 58 nm for 1 and 4 mg/mL, respectively. This is in line with eq 1, where an increase in nanoparticle concentration increases the materials concentration c and thus the constant k_i and film thickness d. The mean roughness σ of the films increased from 0.9 nm for pure PVF to 1.5−2.0 nm in the presence of nanoparticles. The best fits were achieved using thin top and bottom PVF layers with a reduced X-ray scattering length density (SLD), from 11.3 × 10^{-6} $Å^{-2}$ for nominal PVF to 5.5 × 10^{-6} $Å^{-2}$ for the top and substrate/PVF interface. The thicknesses of both additional layers are similar, but it depends on the type of sample, being around 1 nm for the pure PVF film and increasing up to around 3−5 nm for the nanocomposites.

Table 1. Parameters d (Total Film Thickness), σ (Film Roughness), and ρ (PVF Density, Set Constant) Calculated from the XRR-Simulated Profiles for Pure PVF and PVF/FeO_x Nanocomposite Films with Different Nanoparticle Concentration

np concentration (mg/mL)	d (nm)	σ (nm)	ρ (g/cm^3)
0.0	37.4 ± 0.5	0.9 ± 0.1	1.20
1.0	45.8 ± 0.6	1.5 ± 0.5	1.20
4.0	58.2 ± 1.0	2.0 ± 0.6	1.20

For the FeO_x nanoparticles, and also for the ZnO, $LiGdF_4$, and TiO_2 nanoparticles investigated in the last part of the article, we observed a significant decrease of the film thickness as compared to the bare PVF films deposited under similar conditions. We also analyzed CdSe quantum dots (not included in the manuscript) with similar results. The reason why the presence of nanoparticles favors the formation of thinner films is not entirely clear at the moment. Following eq 1, it likely is due to a reduced evaporation rate E caused by the presence of the nanoparticles, which leads to a smaller thin thickness d. It is a phenomenon that will require more attention but was not the aim of the present study.

The topography scan of Figure 2d measured by atomic force microscopy (AFM) corresponds to a region near the film edge of a sample deposited from a 1 mg/mL solution. In this case, the smoothness and uniformity of the film is directly apparent from the AFM image and the corresponding line-scan profile of Figure 2e, complementing the information obtained by XRR. The root-mean-square roughness index (R_q) calculated from the scanned regions was R_q ~0.5−1.0 nm, in very good agreement with the roughness parameter estimated by XRR simulations. The XRR and AFM results show that large-area, homogeneous nanoparticle films with remarkably small mean roughness below 2 nm can be prepared.

https://doi.org/10.1021/acsanm.3c02820
ACS Appl. Nano Mater. 2023, 6, 22651−22659

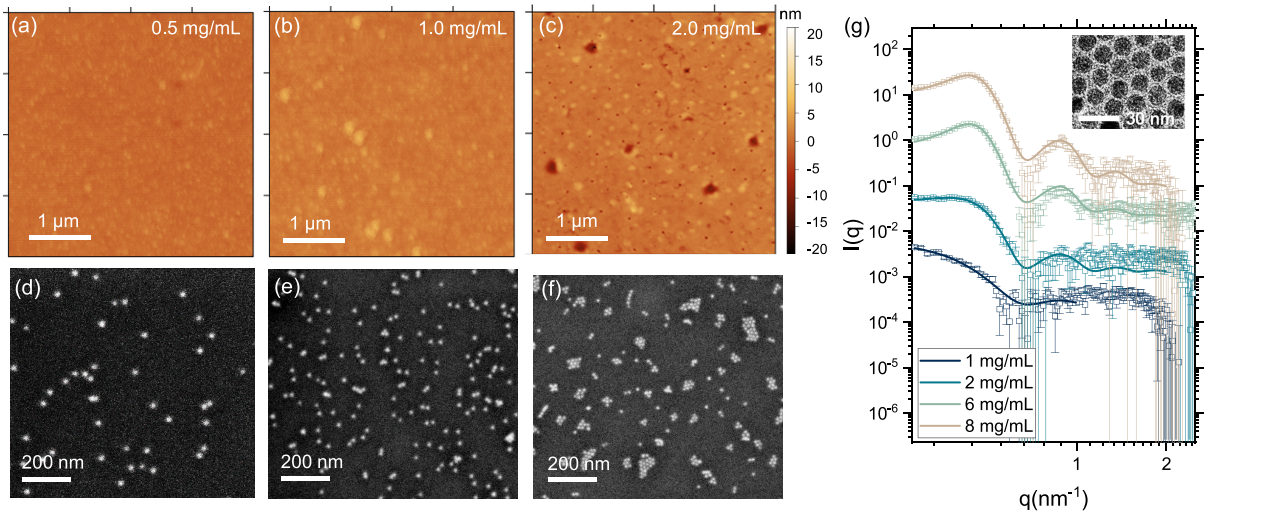

Figure 3. AFM topography scans for thin films from 0.5 wt % PVF solutions and nanoparticle concentrations of (a) 0.5, (b) 1.0, and (c) 2.0 mg/mL. Their corresponding SEM micrographs are depicted in (d), (e), and (f), respectively. (g) 1D-SAXS patterns from single-layer nanocomposites with different nanoparticle concentrations. The inset in (g) shows a TEM image of the assembled particles.

Thin-Film Nanoscale Homogeneity. The prepared large-area thin nanocomposite films are homogeneous on length scales from centimeters down to μm (see Figure S1c). We also investigated the nanoscale homogeneity, in particular the lateral and vertical distribution of nanoparticles within the thin films, by using AFM and SEM. Figure 3a–c shows AFM topography scans of the nanocomposite films with nanoparticle concentrations from 0.5, 1.0 to 2.0 mg/mL. In general, the PVF/OA-FeO_x films are very uniform. Sporadically, small 10 nm-deep pores are observed, which is not uncommon for PVF films[25] as, e.g., in Figure 3c.

Using SEM, the distribution of the nanoparticles within the thin films can be characterized. The corresponding SEM micrographs are presented in Figure 3d–f and Figure S4a–d. With SEM, the average nanoparticle diameter can be determined as 8.0 ± 0.5 nm, which includes both the FeO_x core and the OA ligand shell. We observe that at concentrations of 0.5 and 1 mg/mL, the distribution of the nanoparticles is homogeneous, with a tendency to form 2D-nanoparticle clusters for higher concentrations, such as at 2 mg/mL, and in Figures S3 and S4 for larger concentrations. With the cluster domains, the nanoparticles form ordered 2D hexagonal-close packed (hcp) arrays.

The ∼100 nm cluster assemblies of nanoparticles are observed as mesa structures in the AFM images (Figure 3a–c), or as white nanoparticle multiplets in the SEM images (Figure 3d–f; small white dots are individual particles). Nanoparticles in polymer matrices have a general tendency to form multiplets and clusters with increasing concentration. Figures S10 and S11 show SEM images of nanoparticles with a matrix-compatible PEG-coating where the distribution of the nanoparticles is much more homogeneous, showing the potential of the method to fabricate very homogeneous films.

The presence of cluster domains is in accordance with the increased mean roughness and the need of additional layers with reduced electron density to refine the XRR profile simulations.[30] The nanoparticle area density, which is proportional to the interparticle distance and estimated from large scanned regions, increases linearly with the nanoparticle concentration, as shown in Figure S4e.

The nanoparticle distribution in free-standing thin films was characterized by transmission small-angle X-ray scattering (SAXS). SAXS provides a large-area average of the nanoparticle diameters and homogeneity of the nanoparticle distribution. Figure 3g shows the SAXS intensity curves measured for free-standing films transferred to aluminum O-rings, similar to the sample shown in Figure 1d. The nanoparticle radius determined from the SAXS curves by fitting to a polydisperse sphere model[33] is 6.3 nm. The estimated radius is in agreement with the particles observed by transmission electron microscopy (TEM), shown in the inset of Figure 3g, but smaller compared to the particle radius observed by a 2 keV e-beam in a SEM (8.0 nm). It is because X-ray scattering (and transmission electron microscopy with high energy electrons of 200 kV) is more sensitive to the inorganic FeO_x core rather than the organic shell,[34] with the advantage of averaging a very large number of particles as compared to electron microscopy. The difference of 1.7 nm is in agreement with the thickness of the oleic ligand shell, which is nearly equal to the contour length of the oleic acid molecule.[35] At concentrations equal and larger than 2 mg/mL, we observe a peak in the SAXS-curves at $q \sim 0.4$ nm^{-1} due to the formation of ordered nanoparticle arrays within the clusters, corresponding to ∼16 nm interparticle distance, in agreement with our observations by SEM (with low energy electrons of about 3 kV) and also confirming that the particle cores remain separated by the OA ligand.

The lateral and vertical distribution of the nanoparticles in thin films on Si substrates can be measured by grazing-incidence small-angle X-ray scattering (GISAXS) (see the GISAXS sections in the Supporting Information). The GISAXS-intensity patterns show the formation of single nanocomposite layers on Si, as shown in the Figure S6, confirming the 2D-nanoparticle ordering within the thin film.[34] These results not only are in agreement with the observations obtained from electron microscopy but also reveal the great long-range uniformity since the probing areas for SAXS and GISAXS experiments are of the order from hundreds of micrometers to millimeters.

The tendency to form 2D-nanoparticle clusters can be suppressed by compatibilization of the nanoparticles with the PVF matrix. Figure S9 shows TEM images of iron oxide nanoparticles, which were coated with poly(ethylene oxide)

https://doi.org/10.1021/acsanm.3c02820
ACS Appl. Nano Mater. 2023, 6, 22651−22659

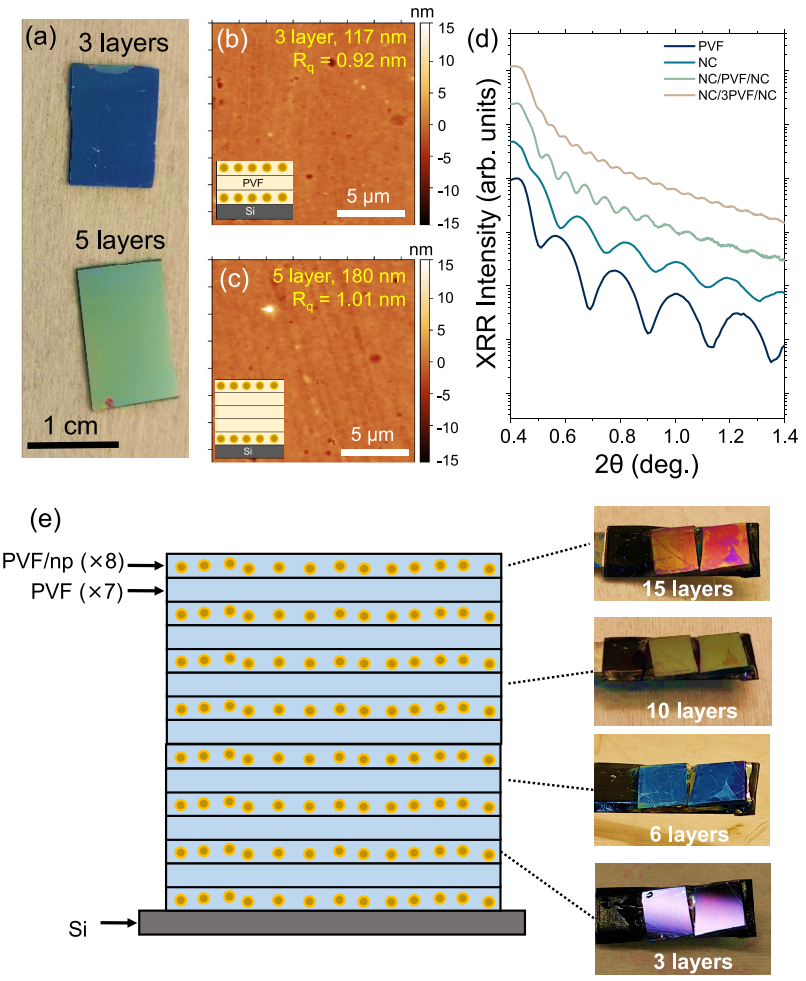

Figure 4. (a) Example of nanocomposite/PVF multilayer structures on Si substrates. AFM topography scans, calculated roughness index (R_q), and sketches of the multilayer structures for (b) three layers and (c) five layers. (d) XRR measurements from the multilayers as well as a single nanocomposite and a PVF reference layer. (e) Example of a heterostructure with a total of 15 stacked nanocomposite/PVF layers on Si.

(PEO) for better compatibility with the PVF matrix. Additionally, Figure S11 shows a 3D reconstuction via electron tomography from a PEO-FeO_x/PVF film and Video S1 displays the resultant reconstruction virtually rotating the film 180° (starting from the side view) where the particles are distributed along the vertical direction. We observe that this considerably reduces 2D-cluster formation but not completely suppresses it since PEO and PVF are only partially miscible.

Thin-Film Multilayer Structures. To prove the versatility of the dip-coating/delamination technique, hetero multilayer structures were fabricated by repeating the transferring process multiple times using alternating nanocomposite (1 mg/mL) and pure PVF films. We note that we refer to multilayers as stacks consisting of multiple delaminated polymer nanocomposite layers and not direct stacks of nanoparticle layers. We note that homomultilayers without PVF can be prepared as well. The uniform interference color exhibited by the multilayers with three and five layers indicates an exceptional thickness control and smoothness, as can be observed in Figure 4a. Figure 4b and c shows the AFM topography scans of the surface of the multilayer structures with three and five layers, respectively. Schematic diagrams of the heterostructures fabricated are also included in the figures together with the calculated R_q of the scanned area ($20 \times 20\ \mu m^2$). The results show that large multilayer films can be prepared with a roughness of the order of 1 nm, similar to that calculated for a single nanocomposite layer with equivalent nanoparticle concentrations (Figure 2c). These observations are confirmed by the XRR measurements, revealing a long-range film uniformity and moderate roughness. The multilayer thickness estimated from the Kiessig fringes[28] are 117 and 180 nm for three and five layers, respectively. This shows that multilayer preparation is an alternative route to adjust the film thickness over a wide range.

Figure 4e shows images of multilayers of up to 15 stacked layers of alternating pure PVF and nanocomposite films. For this film, the magnetic properties due to the magnetic nanoparticles are characterized in detail in the Supporting Information. It is surprising that even for such a large number of layers, the interference color is still uniform, as observed in the photographs of Figure 4e, taken at different stages during the fabrication of the multilayered structure. Such a construction would be difficult to achieve by other methods, revealing the ability to fabricate complex heterostructures for more specific applications in a very short time.

Different Nanoparticle Types. To explore the wider applicability of the dip-coating/delamination technique, we investigated the preparation of similar nanocomposite thin films using nanoparticles of different chemical composition and shape. We therefore investigated ZnO spherical nanoparticles, $LiGdF_4$:Eu (LGF) nanoplatelets, and TiO_2 nanorods (see the

https://doi.org/10.1021/acsanm.3c02820
ACS Appl. Nano Mater. 2023, 6, 22651−22659

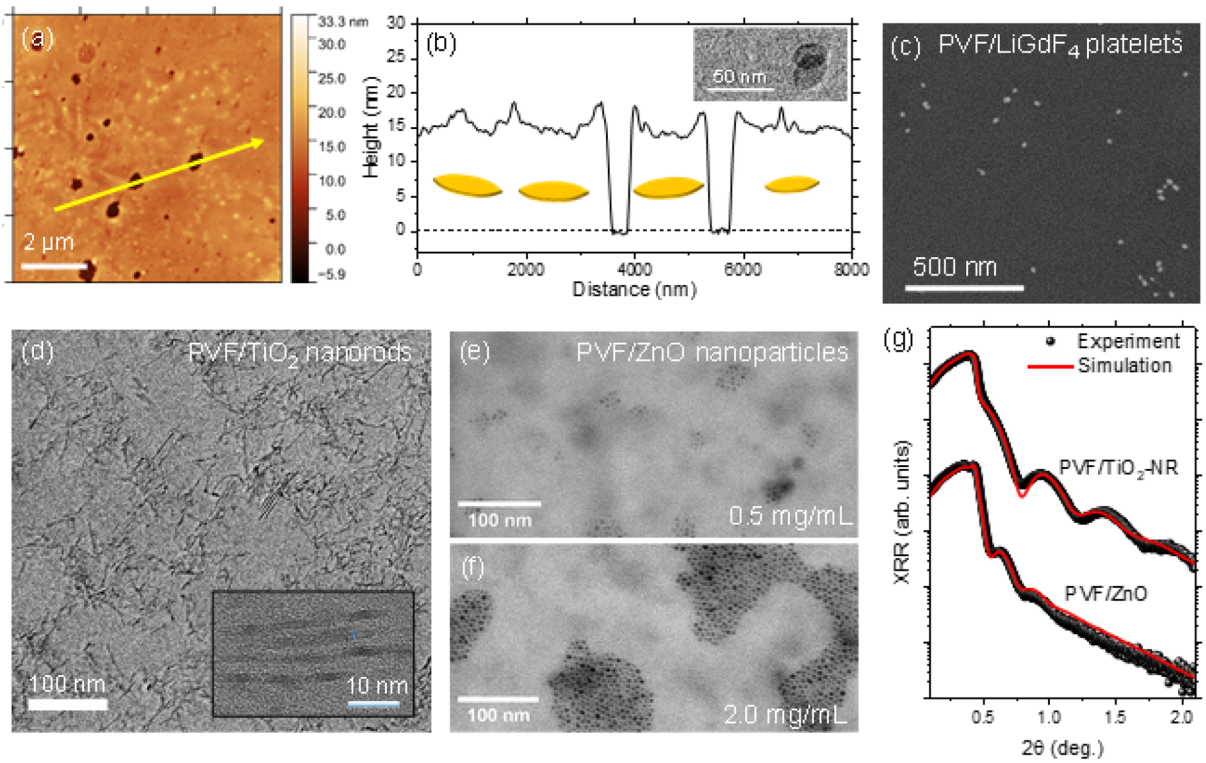

Figure 5. (a) AFM topography scan of a PVF/$LiGdF_4$:Eu nanocomposite. (b) Height profile along the line marked in (a). The inset in (b) shows a TEM micrograph of the platelike particles. (c) SEM image of the nanocomposite with platelets oriented parallel to the substrate. (d) TEM micrograph of the PVF/TiO_2 nanocomposite with 2 mg/mL concentration. The inset in (d) shows a magnification of the rod-like nanostructures. (e) TEM micrograph of the PVF/ZnO nanocomposite with 0.5 and (f) 2.0 mg/mL concentration. (g) Experimental and simulated XRR profiles measured from PVF/TiO_2 (2 mg/mL) and PVF/ZnO (0.5 mg/mL) nanocomposites.

Supporting Information for more details). All of the nanoparticles are stabilized with oleic acid ligand shells. These materials have been chosen because of their application in luminescent, optoelectronic, and sensing devices. LGF is a phosphor material with the ability to convert a single UV photon into multiple visible photons via a quantum cutting process (down-conversion)[36] with applications in mercury-free lamps,[37] and potential in the solar-cell technology.[38] TiO_2 has a wide range of applications, and the high aspect ratio of the 1D structures makes them suitable for photocatalysts,[39] solar cells,[40] and sensors.[21,41,42] ZnO belongs to the family of transparent conductive oxides, with high luminescence efficiency, and therefore it is a relevant material for optoelectronic applications.[43−45] For these nanoparticles, we used a withdrawal speed of 0.25 mm/s to aim at the minimal thickness achievable by film delamination.

Platelets. Figure 5a corresponds to an AFM scan of a PVF nanocomposite film filled with $LiGdF_4$:Eu nanoplatelets. A line-scan profile along the marked arrow is shown in Figure 5b. The inset of Figure 5b displays a micrograph of a PVF/LGF film transferred to a TEM grid where two particles of around 20 × 30 nm^2 are partially overlapping, revealing the platelet shape. The SEM image in Figure 5c shows that the nanoplatelets are oriented parallel to the substrate and the film. The AFM profile in Figure 5b shows small elevations of around 5 nm, in line with a coplanar platelet orientation. Its parallel alignment is a consequence of the capillary flow during the dip-coating process.[46]

Nanorods. Figure 5d shows a TEM micrograph of a PVF film with TiO_2 nanorods (TiO_2-nr) prepared at a concentration of 2 mg/mL. The inset shows a higher magnification of a group of nanorods with dimensions of 30−40 nm length and 2−3 nm diameter. TiO_2-nr is well dispersed within the film covering the entire film area, with structures lying parallel to the Si substrate. We note that the nanocomposite transfer method is more advantageous to deposit large areas of homogeneously distributed nanorods as compared to direct dip-coating of TiO_2-nr on Si substrates (see Figure S8). The film thickness of the PVF/TiO_2-nr nanocomposite was measured by XRR resulting in the profile displayed in Figure 5g. The film thickness determined from XRR simulations is around 30 nm for the TiO_2-nr nanocomposite, demonstrating the ability to fabricate ultrathin nanocomposite films.

ZnO Spheres. Figure 5e and f shows TEM micrographs of PVF/ZnO nanocomposite films prepared at 0.5 and 2.0 mg/mL, respectively. The ZnO nanoparticles have a spherical shape and a diameter of 5 nm. Compared to the FeO_x nanoparticles, the ZnO nanoparticles have a stronger tendency to form 2D clusters of self-assembled hcp nanoparticle monolayers. The film thickness measured by XRR is only 17 nm, as shown in Figure 5g, reflecting the small diameter of the nanoparticles. Additionally, a thicker centimeter-size film, prepared by drop casting the PVF/ZnO solution, shows both high visible-light transmittance and fluorescence under UV irradiation, as shown in Figure S9. Here, it is important to mention that no luminescence quenching was observed, revealing the exceptional stability and compatibility of the nanocomposite.

It has been reported that delamination of such ultrathin ∼10 nm films is not possible or very difficult using untreated substrates or bare PVF;[10] thus, the presence of nanoparticles, even at low densities, favors the conditions required to delaminate the film through the film−water interface (e.g.,

https://doi.org/10.1021/acsanm.3c02820
ACS Appl. Nano Mater. 2023, 6, 22651−22659

film strain, adhesion, and interface energy), easing the fabrication of ultrathin PVF-based films.[10,47]

With respect to magnetic materials, the proposed method is an interesting alternative TEM sample preparation method to prevent magnetic materials from escaping into the electron microscope column during irradiation by the electron beam.[48]

Due to the ease to produce monolayers of particles with medium to long interparticle distance, it means that similar films can be used as anisotropic conductive films[49] with an appropriate filler material. Also, absorbing layers, UV-protective films, or downconverting layers for solar cells can be readily tested without influencing the fabrication process of the devices. Similar to both novel mild acid-assisted transfer-printing method and dipping-embedded-transfer method proposed by Fan et al.,[12,50,51] the compatibility of this approach with the commonly used PEDOT:PSS materials would be of interest for flexible and conformable electronics.

CONCLUSIONS AND OUTLOOK

In conclusion, a versatile, well-controllable, and scalable methodology to fabricate ultrathin nanocomposite films on different types of substrates and shapes is proposed, with a roughness of the order of few nanometers and great film uniformity. For the standard 2.5 × 2.5 cm^2 ultrathin films, aspect ratios of up to 10^6 can be achieved. The method has been used to fabricate uniform multilayer structures as well as nanocomposites with other material fillers relevant because of their magnetic and optoelectronic properties such as FeO_x nanoparticles, down-conversion $LiGdF_4$:Eu platelets, photocatalytic TiO_2 nanorods, or luminescent ZnO spherical nanoparticles. We show that the magnetic and optical properties of the nanoparticles are well preserved by the fabrication method. The simplicity of the method and quality of the fabricated films allow for a rapid fabrication of functional devices. One of the advantages of the method proposed here is the simplicity to prepare solutions and films with no special atmosphere conditions, in simple steps, very quickly, and with minimal material waste.

ASSOCIATED CONTENT

Supporting Information

The Supporting Information is available free of charge at https://pubs.acs.org/doi/10.1021/acsanm.3c02820.

Experimental section; thin-film optical characterization; thin-film AFM and SEM analyses; thin-film GISAXS; thin-film magnetic characterization; additional nanocomposite systems (PDF)

Resultant reconstruction virtually rotating the film to 180° (starting from the side view) where the particles are distributed along the vertical direction (MP4)

AUTHOR INFORMATION

Corresponding Authors

G. Cristian Vásquez − *Jülich Centre for Neutron Science (JCNS-1/IBI-8), Forschungszentrum Jülich, Jülich 52425, Germany*; Email: c.vasquez@fz-juelich.de

Stephan Förster − *Jülich Centre for Neutron Science (JCNS-1/IBI-8), Forschungszentrum Jülich, Jülich 52425, Germany; Institute of Physical Chemistry, RWTH Aachen University, Aachen 52074, Germany*; orcid.org/0000-0002-7323-2449; Email: s.foerster@fz-juelich.de

Authors

Martin Dulle − *Jülich Centre for Neutron Science (JCNS-1/IBI-8), Forschungszentrum Jülich, Jülich 52425, Germany*

Beate Förster − *Jülich Centre for Neutron Science (JCNS-1/IBI-8), Forschungszentrum Jülich, Jülich 52425, Germany; Ernst Ruska-Centre for Microscopy and Spectroscopy with Electrons (ER-C 1), Forschungszentrum Jülich, Jülich 52425, Germany*; orcid.org/0000-0002-8464-4473

Margarita Kruteva − *Jülich Centre for Neutron Science (JCNS-1/IBI-8), Forschungszentrum Jülich, Jülich 52425, Germany*; orcid.org/0000-0002-7686-0934

Sascha Ehlert − *Jülich Centre for Neutron Science (JCNS-1/IBI-8), Forschungszentrum Jülich, Jülich 52425, Germany*

Complete contact information is available at: https://pubs.acs.org/10.1021/acsanm.3c02820

Author Contributions

The manuscript was written through contributions of all authors. All authors have given approval to the final version of the manuscript.

Funding

Financial support by Forschungszentrum Jülich is gratefully acknowledged.

Notes

The authors declare no competing financial interest.

ACKNOWLEDGMENTS

G.C.V. acknowledges the Tasso Springer Fellowship program supported by JCNS and Forschunszentrum Jülich. G.C.V. also thanks Dr. Connie Bednarski-Meinke for assistance during AFM measurements and O. Petracic for helpful discussion on the magnetic characterization.

REFERENCES

(1) Forrest, S. R. The Path to Ubiquitous and Low-Cost Organic Electronic Appliances on Plastic. *Nature* **2004**, *428* (6986), 911−918.

(2) Saveleva, M. S.; Eftekhari, K.; Abalymov, A.; Douglas, T. E. L.; Volodkin, D.; Parakhonskiy, B. V.; Skirtach, A. G. Hierarchy of Hybrid Materials—The Place of Inorganics-in-Organics in It, Their Composition and Applications. *Front. Chem.* **2019**, *7*, 179.

(3) Sanchez, C.; Julián, B.; Belleville, P.; Popall, M. Applications of Hybrid Organic−Inorganic Nanocomposites. *J. Mater. Chem.* **2005**, *15* (35−36), 3559.

(4) Fan, X.; Nie, W.; Tsai, H.; Wang, N.; Huang, H.; Cheng, Y.; Wen, R.; Ma, L.; Yan, F.; Xia, Y. PEDOT:PSS for Flexible and Stretchable Electronics: Modifications, Strategies, and Applications. *Advanced Science* **2019**, *6* (19), 1900813.

(5) Fan, X. Doping and Design of Flexible Transparent Electrodes for High-Performance Flexible Organic Solar Cells: Recent Advances and Perspectives. *Adv. Funct. Mater.* **2021**, *31* (8), 2009399.

(6) Gong, M.; Zhang, L.; Wan, P. Polymer Nanocomposite Meshes for Flexible Electronic Devices. *Prog. Polym. Sci.* **2020**, *107*, No. 101279.

(7) Rawat, M.; Jayaraman, E.; Balasubramanian, S.; Iyer, S. S. K. Organic Solar Cells on Paper Substrates. *Adv. Mater. Technol.* **2019**, *4* (8), 1900184.

(8) Zeng, J.; Matsusaki, M. Layer-by-Layer Assembly of Nanofilms to Control Cell Functions. *Polym. Chem.* **2019**, *10* (23), 2960−2974.

(9) Kozlovskaya, V.; Dolmat, M.; Kharlampieva, E. Two-Dimensional and Three-Dimensional Ultrathin Multilayer Hydrogels through Layer-by-Layer Assembly. *Langmuir* **2022**, *38* (26), 7867−7888.

(10) Baxamusa, S. H.; Stadermann, M.; Aracne-Ruddle, C.; Nelson, A. J.; Chea, M.; Li, S.; Youngblood, K.; Suratwala, T. I. Enhanced Delamination of Ultrathin Free-Standing Polymer Films via Self-Limiting Surface Modification. *Langmuir* **2014**, *30* (18), 5126−5132.

(11) Hall, D. B.; Underhill, P.; Torkelson, J. M. Spin Coating of Thin and Ultrathin Polymer Films. *Polym. Eng. Sci.* **1998**, *38* (12), 2039−2045.
(12) Fan, X.; Xu, B.; Liu, S.; Cui, C.; Wang, J.; Yan, F. Transfer-Printed PEDOT:PSS Electrodes Using Mild Acids for High Conductivity and Improved Stability with Application to Flexible Organic Solar Cells. *ACS Appl. Mater. Interfaces* **2016**, *8* (22), 14029−14036.
(13) Stafford, C. M.; Roskov, K. E.; Epps, T. H.; Fasolka, M. J. Generating Thickness Gradients of Thin Polymer Films via Flow Coating. *Rev. Sci. Instrum.* **2006**, *77* (2), No. 023908.
(14) Davis, R. L.; Jayaraman, S.; Chaikin, P. M.; Register, R. A. Creating Controlled Thickness Gradients in Polymer Thin Films via Flowcoating. *Langmuir* **2014**, *30* (19), 5637−5644.
(15) Mittal, M.; Niles, R. K.; Furst, E. M. Flow-Directed Assembly of Nanostructured Thin Films from Suspensions of Anisotropic Titania Particles. *Nanoscale* **2010**, *2* (10), 2237.
(16) Yuan, H.; Zvonkina, I. J.; Al-Enizi, A. M.; Elzatahry, A. A.; Pyun, J.; Karim, A. Facile Assembly of Aligned Magnetic Nanoparticle Chains in Polymer Nanocomposite Films by Magnetic Flow Coating. *ACS Appl. Mater. Interfaces* **2017**, *9* (12), 11290−11298.
(17) Song, B.; Zhang, L.; Sun, J.; Lam, J. W. Y.; Tang, B. Z. In Situ Synthesis of AIEgen-based Porous Organic Polymer Films by Interfacial Amino-yne Click Polymerization for Efficient Light-Harvesting. *Angew. Chem., Int. Ed.* **2023**, *62* (18), No. e202302543.
(18) Yang, Y.; Chen, Y.; Izquierdo-Ruiz, F.; Schäfer, C.; Rahm, M.; Börjesson, K. A Self-Standing Three-Dimensional Covalent Organic Framework Film. *Nat. Commun.* **2023**, *14* (1), 220.
(19) Ottomaniello, A.; Vezio, P.; Tricinci, O.; Den Hoed, F. M.; Dean, P.; Tredicucci, A.; Mattoli, V. Highly Conformable Terahertz Metasurface Absorbers via Two-Photon Polymerization on Polymeric Ultra-Thin Films. *Nanophotonics* **2023**, *12* (8), 1557−1570.
(20) Barsotti, J.; Rapidis, A. G.; Hirata, I.; Greco, F.; Cacialli, F.; Mattoli, V. Ultrathin, Ultra-Conformable, and Free-Standing Tattooable Organic Light-Emitting Diodes. *Adv. Electron Mater.* **2021**, *7* (3), 2001145.
(21) Thangamani, G. J.; Pasha, S. K. K. Titanium Dioxide (TiO2) Nanoparticles Reinforced Polyvinyl Formal (PVF) Nanocomposites as Chemiresistive Gas Sensor for Sulfur Dioxide (SO2) Monitoring. *Chemosphere* **2021**, *275*, No. 129960.
(22) Knapczyk, J. W. Vinyl Acetal Polymers. In *Kirk-Othmer Encyclopedia of Chemical Technology*; John Wiley & Sons, Inc.: Hoboken, NJ, USA, 2000. DOI: 10.1002/0471238961.2209142511140116.a01.
(23) Lian, F.; Guan, H.; Wen, Y.; Pan, X. Polyvinyl Formal Based Single-Ion Conductor Membranes as Polymer Electrolytes for Lithium Ion Batteries. *J. Membr. Sci.* **2014**, *469*, 67−72.
(24) Zhang, H.; Lian, F.; Bai, L.; Meng, N.; Xu, C. Developing Lithiated Polyvinyl Formal Based Single-Ion Conductor Membrane with a Significantly Improved Ionic Conductivity as Solid-State Electrolyte for Batteries. *J. Membr. Sci.* **2018**, *552*, 349−356.
(25) Barsotti, J.; Hirata, I.; Pignatelli, F.; Caironi, M.; Greco, F.; Mattoli, V. Ultraconformable Freestanding Capacitors Based on Ultrathin Polyvinyl Formal Films. *Adv. Electron Mater.* **2018**, *4* (11), 1800215.
(26) Viola, F. A.; Barsotti, J.; Melloni, F.; Lanzani, G.; Kim, Y.-H.; Mattoli, V.; Caironi, M. A Sub-150-Nanometre-Thick and Ultra-conformable Solution-Processed All-Organic Transistor. *Nat. Commun.* **2021**, *12* (1), 5842.
(27) Mohanapriya, M. K.; Deshmukh, K.; Kumar Sadasivuni, K.; Thangamani, G.; Chidambaram, K.; Basheer Ahamed, M.; Khadheer Pasha, S. K. Enhanced Quality Factor of Polyvinyl Formal (PVF) Based Nanocomposites Filled with Zinc Oxide and Carbon Black Nanoparticles for Wireless Sensing Applications. *Mater. Today Proc.* **2019**, *9*, 199−216.
(28) Miyata, N.; Miyazaki, T. Relatively Thick (Few Micrometers) Film Structure Estimated by Back-Incidence Neutron Reflectometry. *Physica B Condens Matter* **2018**, *551*, 449−451.
(29) Björck, M.; Andersson, G. GenX: An Extensible X-Ray Reflectivity Refinement Program Utilizing Differential Evolution. *J. Appl. Crystallogr.* **2007**, *40* (6), 1174−1178.
(30) Konefał, M.; Černoch, P.; Patsula, V.; Pavlova, E.; Dybal, J.; Załęski, K.; Zhigunov, A. Enhanced Ordering of Block Copolymer Thin Films upon Addition of Magnetic Nanoparticles. *ACS Appl. Mater. Interfaces* **2021**, *13* (7), 9195−9205.
(31) Bindini, E.; Naudin, G.; Faustini, M.; Grosso, D.; Boissière, C. Critical Role of the Atmosphere in Dip-Coating Process. *J. Phys. Chem. C* **2017**, *121* (27), 14572−14580.
(32) Faustini, M.; Louis, B.; Albouy, P. A.; Kuemmel, M.; Grosso, D. Preparation of Sol−Gel Films by Dip-Coating in Extreme Conditions. *J. Phys. Chem. C* **2010**, *114* (17), 7637−7645.
(33) Rosenfeld, Y. Free-Energy Model for the Inhomogeneous Hard-Sphere Fluid in D Dimensions: Structure Factors for the Hard-Disk (D = 2) Mixtures in Simple Explicit Form. *Phys. Rev. A (Coll Park)* **1990**, *42* (10), 5978−5989.
(34) Mishra, D.; Greving, D.; Badini Confalonieri, G. A.; Perlich, J.; Toperverg, B. P.; Zabel, H.; Petracic, O. Growth Modes of Nanoparticle Superlattice Thin Films. *Nanotechnology* **2014**, *25* (20), 205602.
(35) Fu, Z.; Xiao, Y.; Feoktystov, A.; Pipich, V.; Appavou, M.-S.; Su, Y.; Feng, E.; Jin, W.; Brückel, T. Field-Induced Self-Assembly of Iron Oxide Nanoparticles Investigated Using Small-Angle Neutron Scattering. *Nanoscale* **2016**, *8* (43), 18541−18550.
(36) Wegh, R. T.; Donker, H.; Oskam, K. D.; Meijerink, A. Visible Quantum Cutting in LiGdF 4:Eu 3+ Through Downconversion. *Science (1979)* **1999**, *283* (5402), 663−666.
(37) Feldmann, C.; Jüstel, T.; Ronda, C. R.; Wiechert, D. U. Quantum Efficiency of Down-Conversion Phosphor LiGdF4:Eu. *J. Lumin.* **2001**, *92* (3), 245−254.
(38) Kim, S. Y.; Won, Y.-H.; Jang, H. S. A Strategy to Enhance Eu3+ Emission from LiYF4:Eu Nanophosphors and Green-to-Orange Multicolor Tunable, Transparent Nanophosphor-Polymer Composites. *Sci. Rep* **2015**, *5* (1), 7866.
(39) Schneider, J.; Matsuoka, M.; Takeuchi, M.; Zhang, J.; Horiuchi, Y.; Anpo, M.; Bahnemann, D. W. Understanding TiO 2 Photocatalysis: Mechanisms and Materials. *Chem. Rev.* **2014**, *114* (19), 9919−9986.
(40) García-Tecedor, M.; Karazhanov, S. Z.; Vásquez, G. C.; Haug, H.; Maestre, D.; Cremades, A.; Taeño, M.; Ramírez-Castellanos, J.; González-Calbet, J. M.; Piqueras, J.; You, C. C.; Marstein, E. S. Silicon Surface Passivation by PEDOT: PSS Functionalized by SnO 2 and TiO 2 Nanoparticles. *Nanotechnology* **2018**, *29* (3), No. 035401.
(41) Karunagaran, B.; Uthirakumar, P.; Chung, S. J.; Velumani, S.; Suh, E.-K. TiO2 Thin Film Gas Sensor for Monitoring Ammonia. *Mater. Charact* **2007**, *58* (8−9), 680−684.
(42) Choi, Y. J.; Seeley, Z.; Bandyopadhyay, A.; Bose, S.; Akbar, S. A. Aluminum-Doped TiO2 Nano-Powders for Gas Sensors. *Sens Actuators B Chem.* **2007**, *124* (1), 111−117.
(43) Kumar, R.; Nordseth, Ø.; Vásquez, G. C.; Foss, S. E.; Monakhov, E.; Svensson, B. G. Investigation of N-Al:ZnO/p-Cu2O Heterojunction for c-Si Tandem Heterojunction Solar Cell Applications. *AIP Conf. Proc.* **2019**, *2147*, 130002.
(44) Wang, H.; Qiu, X.; Liu, W.; Fu, F.; Yang, D. A Novel Lignin/ZnO Hybrid Nanocomposite with Excellent UV-Absorption Ability and Its Application in Transparent Polyurethane Coating. *Ind. Eng. Chem. Res.* **2017**, *56* (39), 11133−11141.
(45) Shanshool, H. M.; Yahaya, M.; Yunus, W. M. M.; Abdullah, I. Y. Investigation of Energy Band Gap in Polymer/ZnO Nanocomposites. *Journal of Materials Science: Materials in Electronics* **2016**, *27* (9), 9804−9811.
(46) Feng, J.; Xia, H.; You, F.; Mao, H.; Ma, X.; Tao, H.; Zhao, X.; Wang, M.-C. Alignment of Ag Nanowires on Glass Sheet by Dip-Coating Technique. *J. Alloys Compd.* **2018**, *735*, 607−612.
(47) Ma, J.; Kim, J. M.; Hoque, M. J.; Thompson, K. J.; Nam, S.; Cahill, D. G.; Miljkovic, N. Role of Thin Film Adhesion on Capillary Peeling. *Nano Lett.* **2021**, *21* (23), 9983−9989.
(48) Bian, L.; Cao, Q.; Zheng, L.; Liu, Y. Ultramicrotomy Preparation of Magnetic Nanoparticles for Transmission Electron Microscopy. *Ultramicroscopy* **2021**, *227*, No. 113275.

(49) Hwang, H.; Kong, M.; Kim, K.; Park, D.; Lee, S.; Park, S.; Song, H.-J.; Jeong, U. Stretchable Anisotropic Conductive Film (S-ACF) for Electrical Interfacing in High-Resolution Stretchable Circuits. *Sci. Adv.* **2021**, *7* (32), No. eabh0171.
(50) Fan, X.; Xu, B.; Wang, N.; Wang, J.; Liu, S.; Wang, H.; Yan, F. Highly Conductive Stretchable All-Plastic Electrodes Using a Novel Dipping-Embedded Transfer Method for High-Performance Wearable Sensors and Semitransparent Organic Solar Cells. *Adv. Electron. Mater.* **2017**, *3* (5), 1600471.
(51) Fan, X.; Stott, N. E.; Zeng, J.; Li, Y.; Ouyang, J.; Chu, L.; Song, W. PEDOT:PSS Materials for Optoelectronics, Thermoelectrics, and Flexible and Stretchable Electronics. *J. Mater. Chem. A Mater.* **2023**, *11* (35), 18561−18591.

https://doi.org/10.1021/acsanm.3c02820
ACS Appl. Nano Mater. 2023, 6, 22651−22659